Dynamic stall at high Reynolds numbers due to variant types of airfoil motion

Dynamic stall at high Reynolds numbers due to variant types of airfoil motion

J Kiefer[1], C E Brunner[2], M Hultmark[2] and M O L Hansen[1]

[1] Department of Wind Energy, Technical University of Denmark, Kgs. Lyngby, Denmark
[2] Department of Mechanical and Aerospace Engineering, Princeton University, Princeton, New Jersey, USA

E-mail: molh@dtu.dk

Abstract. Unsteady airfoil experiments were conducted in a high-pressure wind tunnel at chord Reynolds numbers of $Re_c = 3.0 \times 10^6$. A moderately thick NACA0021 airfoil was pitched from rest beyond the static stall angle in six individual ramp tests with increasing and decreasing angles of attack. The variant types of motion of the pitching maneuvers were characterized by constant angular velocity, angular acceleration and angular jerk, respectively. The ramp-up experiments revealed a substantial and time-dependent excess of the aerodynamic forces from static values in all three test cases and exhibited a distinct time delay as a consequence of the variant motion types. Similarly, the ramp-down experiments were largely impacted by the progression of the pitching motion, resulting in pronounced differences in the temporal development of lift and drag. Results are shown as time series of integrated forces and surface pressure distributions.

1. Introduction

During operation, wind turbines are perpetually exposed to unsteady conditions of varying characteristics. The unsteadiness of the aerodynamics can originate from, for example, turbulence in the atmospheric boundary layer, velocity shear from the wake of a preceding wind turbine upstream, or other unsteady phenomena. Vibrations of the blade, azimuthal blade position and tower passage add to the complexity and unsteadiness of the flow field. At blade element level, the dynamic and unsteady inflow can be characterized as a sudden change in inflow velocity and in angle of attack, often in excess of the static stall angle, which results in a large lift and drag overshoot. This is referred to as dynamic stall, which is often described as an open research question, especially at high Reynolds numbers [1].

Experiments and simulations of this phenomenon have been conducted for over sixty years, particularly in the context of helicopter aerodynamics, but have mainly been focused on continuous sinusoidal pitching motions. Fewer studies have been conducted on simpler motion profiles, such as a linear increase of the angle of attack. Gupta and Ansell conducted a thorough experimental investigation of an airfoil pitching at a constant rate and a Reynolds number of $Re_c = 0.5 \times 10^6$ in reference [2]. Pressure measurements as well as particle image velocimetry revealed a laminar separation bubble on the untripped airfoil, which initiated the lift collapse with its breakdown at higher angles of attack. Direct numerical simulations were carried out by Rosti et al. [3] at a chord Reynolds number of 20 000. The nearly linear increase in lift during the constant pitch rate maneuver was followed by an oscillating lift value corresponding

to alternating vortex shedding from the leading and trailing edge of the airfoil. In the 1990s, researchers at the University of Glasgow conducted a series of unsteady experiments on various airfoil geometries spanning a large parameter space. A selection of the findings is reported in the G.U. Aero Report 9209 by Galbraith et al. [4], which covers more than 150 different ramp-up and ramp-down tests conducted with a NACA0015 airfoil including variations in starting and finishing angle, pitch rate, and at Reynolds numbers up to $Re_c = 2 \times 10^6$. The results are presented as pressure and force time series.

As wind turbines consistently grow larger with every new generation, a critical parameter in the aim to attain full dynamic similarity is the Reynolds number. To experimentally attain a high Reynolds number in a conventional wind tunnel, commonly the velocity or the length scale of the model is increased. Both approaches work well in static airfoil tests, but become hindering when conducting experiments in unsteady conditions at high Reynolds numbers due to the inverse relationship of the Reynolds number $Re_c = \rho\, U_\infty\, c\, \mu^{-1}$ and the reduced frequency $k = \pi\ f\ c\ U_\infty^{-1}$, with respect to the free-stream velocity U_∞. For periodic inflow conditions, the aerodynamics are typically characterized by the reduced frequency. However, for non-periodic motions, the reduced time $t^* = 2\ U_\infty\ t\ c^{-1}$ is commonly used as a substitute. As is usual, the semi-chord length $c/2$ is used as the characteristic length scale in the reduced frequency and the reduced time [5]. In the above formulas, ρ depicts the fluid density, c is the chord length of the airfoil, μ is the dynamic viscosity of the fluid, f is the dimensional pitching frequency and t is the dimensional time.

2. Experimental Setup

The unsteady airfoil tests were conducted in a specialized high-pressure flow facility named the High Reynolds number Test Facility (HRTF) located at Princeton University. This closed-loop wind tunnel can be pressurized up to a static pressure of $p_0 = 230$ atm and can attain free-stream velocities up to $U_\infty = 10$ m/s, where the working fluid is dry air. Flow conditioning and a 2.2:1 contraction ratio result in a free-stream turbulence between 0.3 and 1.1% inside the circular test section [6], where the highest free-stream turbulence occurs at the highest Reynolds numbers. The test section measures 0.5 m in diameter and 4.9 m in total length. The free-stream velocity was measured approximately 1.5 m upstream of the leading-edge of the airfoil with a conventional Pitot-static tube connected to a Validyne DP-15 differential pressure transducer with a range of ± 2 psi. Further details on the facility including a photograph and a sketch can be found in references [7] and [8].

A symmetric NACA0021 airfoil with 21% relative thickness, a chord length of $c = 0.17$ m and an aspect ratio of $AR = 1.5$ was used as the test model for this study. To reduce end-effects on the finite span airfoil in the circular test section of the wind tunnel, the airfoil was equipped with elliptical endplates (see figure 1). A total of 32 pressure taps were press-fitted into the airfoil surface on both the suction and pressure side. Each tap was connected via 0.25 m long Urethane tubing to an individual, temperature-compensated pressure transducer (Honeywell HSC) located on a custom-made circuit board inside the airfoil (figure 1). The 32 pressure transducers were sampled with four 8-channel hardware-timed multiplexers at a rate of 420 Hz, which resulted in 150 sampled pressure distributions within the time period of airfoil motion.

Forces and moments in all three spatial dimensions were recorded with a JR3 load cell with a range of ± 200 N. The angle of attack variation around the rotation axis at half chord was executed by a stepper motor. The motor was connected through a worm gear to a rotary table, on which the airfoil assembly was mounted. Concurrently, the instantaneous angle of attack was measured with a capacitive encoder (CUI AMT103) attached to the stepper motor shaft. Self-retention of the worm gear prevented the undesired change in angle of attack by aerodynamic moments. All data were sampled at 10 kHz.

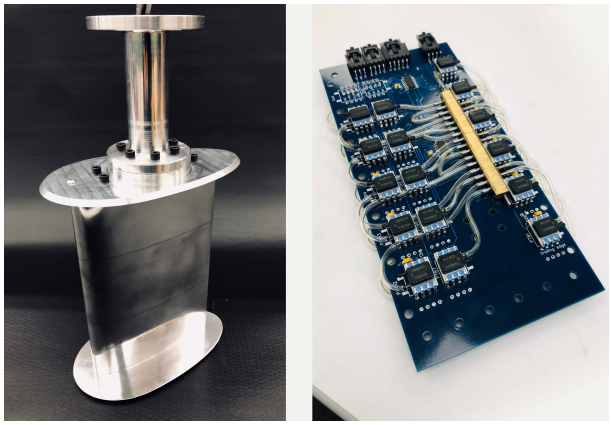

Figure 1. *Left:* The NACA0021 test airfoil section with 32 pressure taps, two elliptical endplates and the attached mounting rod. *Right:* Circuit board with 16 visible Honeywell HSC pressure transducers, four embedded 8-channel multiplexers and a static-pressure manifold for reference.

3. Approach

The airfoil tests were carried out at a free-stream velocity of merely 1.9 m/s and a static tunnel pressure of approximately 20.7 MPa (approximately 206 bar) to achieve a chord Reynolds number of $Re_c = 3.0 \times 10^6$. The low velocity allows pitching rates to be experimentally attainable by keeping dimensional time-scales relatively long, which also enables time resolved measurements of the pressure distribution using conventional pressure sensors.

Both pitch-up and pitch-down cases were systematically tested for different pitching motions. For the pitch-up test cases, the airfoil was at rest at a constant angle of attack of $\alpha = 17°$ before the pitching motion initiated at $t^* = 0$. The three pitching motions all execute the change in angle of attack over a non-dimensional time interval of $\Delta t^* = 31.7$. The three motions are characterized by constant angular velocity $\dot{\alpha} = 21.4\ °/s$, constant angular acceleration $\ddot{\alpha}$, and constant angular jerk $\dddot{\alpha}$, respectively (see figure 2a). In the remainder of the article, the pitching motions will be interchangeably referred to as test cases 1, 2 and 3, or linear, quadratic and cubic test cases in the pitch-up and pitch-down experiments. The airfoil remained at $\alpha = 32°$ after the pitching-motions were completed and data were recorded until lift and drag values reached their time-independent values. The motions were reversed for the pitch-down test cases, but featured the same motion characteristics, as the pitch-up cases, with an initial angle of attack of $\alpha = 32°$ and a final angle of attack of $\alpha = 17°$ (see figure 4a). For all test cases, the presented data depicts the phase-average of 150 individual pitching maneuvers. No corrections for blockage or aspect ratio were applied to the data.

4. Results

The six test cases for the pitch-up and pitch-down experiments are presented in figures 2 and 4, where the geometric angle of attack α, the lift coefficient, and the drag coefficient are plotted over the non-dimensional time t^*. The lift and drag coefficients shown in these plots were computed from the integrated surface pressures obtained by the pressure-sensor array embedded in the airfoil surface. The drag values thus depict only the pressure drag contribution to the total drag and neglect skin friction.

The shaded areas or background colors in all following plots correspond to the period of airfoil motion. White represents the airfoil at rest at its minimum angle of attack of $\alpha = 17°$ with an attached or reattaching flow field. Light gray implies that the airfoil is rotating around its pitching axis at the pitching rate indicated by the individual line type as shown in the legend. Dark grey indicates that the airfoil is at a constant, maximum angle of attack of $\alpha = 32°$ with a separating or largely separated flow field. The colored markers identify points in time, at which the airfoil surpasses the static angle of attack $\alpha_s = 24.5°$.

4.1. Pitch-up motion

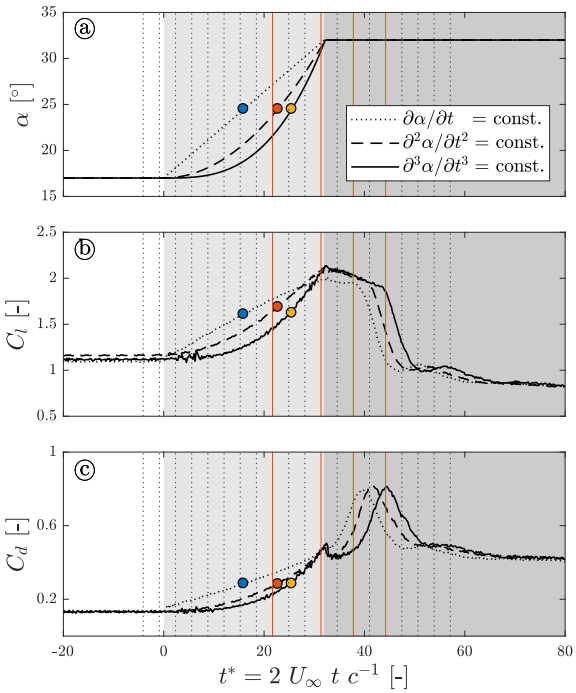

Figure 2. a) The geometric angle of attack α over the non-dimensional time $t^* = 2\ U_\infty\ t\ c^{-1}$ for three different motion profiles. Plots b) and c) show the lift and drag coefficients C_l and C_d over time t^* integrated from the experimentally obtained surface-pressure distribution over the airfoil. Colored circles indicate the point in time, when the static stall angle is surpassed. The legend in a) characterizes the motions during the time period highlighted in light gray and applies to all plots. Red vertical lines indicate moments in time for which the instantaneous pressure distributions are shown in figure 6a-d.

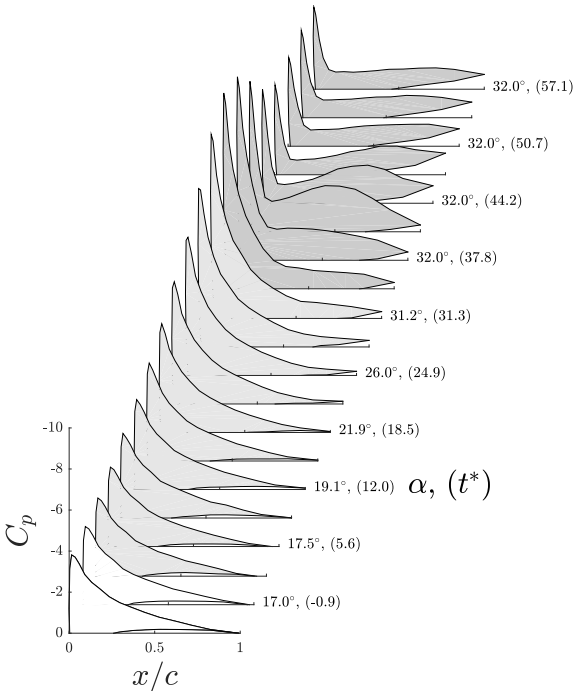

Figure 3. Time series of the suction-side pressure distribution for the quadratic motion profile, where the angular acceleration $\partial^2\alpha/\partial t^2 = \text{const.}$ between $0 \leq t^* \leq 31.7$. The color shades correspond to the same time periods highlighted in figure 2. The third axis shows the instantaneous geometric angle of attack α as well as the reduced time t^* in parentheses.

The following observations are valid for all three test cases. During the ramp-up maneuver, lift and drag increase proportionally to the change in angle of attack, indicating an immediate adoption of the pressure distribution to the instantaneous angle of attack. Up to approximately $\alpha = 28°$, all three test cases exhibit a nearly identical pressure distribution at the same angle of attack, independent of the instantaneous pitch rate $\partial\alpha/\partial t$. Beyond this angle, the pressure distributions show a suction plateau forming in the back part of the airfoil, suggesting flow reversal and subsequent turbulent boundary layer separation. The separation point moves forward with increasing time t^*, which leads to an enlarged plateau in the pressure distribution.

The highest angle of attack of $\alpha = 32°$ is reached at time $t^* = 31.7$, when all test cases attain the highest lift value during the pitching maneuver. While the angle of attack remains constant at times greater than $t^* > 31.7$, the lift decays only slightly and is accompanied by a rapid increase in drag. In this time period, the suction peak near the leading-edge narrows

and decreases in magnitude. Simultaneously, the pressure distributions exhibit a growing bulge in the back 85% of the airfoil indicating an intensifying low pressure region in the flow field, as shown in figures 6c and d. The increase in suction likely stems from a growing shear-layer vortex forming above the airfoil. The separation point, visible as a saddle point in the pressure distribution between the leading-edge suction peak and the vortex bulge moves forward.

A maximum in the drag value commences the subsequent collapse in lift, implying the strongest impact of the suction of the vortex on the airfoil. The simultaneous collapse in lift and drag is visible in the pressure distributions as a decrease in leading-edge suction in combination with the secondary suction peak moving aft (figure 3). The latter suggests the release and convection of the shear-layer vortex downstream. The airfoil eventually experiences largely separated flow on the suction side, where the separation point comes to rest at approximately $x/c = 0.1$ after the pressure fluctuation has passed.

Throughout the time series and for all test cases, the suction peak near the leading-edge is sustained, suggesting a constantly attached flow around the leading-edge of the airfoil. The data provides no evidence for a commonly observed vortex separation at the leading-edge. Instead a vortex forms further downstream with its core initially located at approximately half chord. Presumably, the relatively blunt leading-edge of the moderately thick airfoil facilitates the attached flow to maintain the pressure peak. At the same Reynolds number, a sharper leading-edge would therefore promote an earlier separation with respect to the chord length and vice versa for a thick airfoil with a blunt leading-edge, where attached flow might be sustained past the quarter chord. Furthermore, the pressure distributions do not indicate the presence of a laminar separation bubble at this Reynolds number.

When comparing the three pitching motions, the most notable difference is the varying duration from the completion of the pitching motion until the onset of stall. Since the duration or the delay time until stall onset, respectively, varies between all three test cases, its cause must be related to a point in time prior to the completion of the pitching motion. Hence, the flow field development must be significantly dependent on the temporal change of the pitching maneuver, since all other commonly used parameters to describe unsteady airfoil motion, such as the pitching amplitude, mean angle, the reduced frequency and the Reynolds number, were kept constant. Plots a-d in figure 6 show the chronological development of the pressure distributions for the three ramp-up test cases and indicate flow reversal and earlier boundary layer separation in the linear ramp case compared to the two other cases (figure 6b). Similarly, the boundary layer in the quadratic ramp case separates before the cubic case with respect to the non-dimensional time t^*. The selected points in time shown in figure 6 are denoted as red vertical lines in figure 2 as reference. Consequently, the difference in duration develops during ramp-up maneuver and carries through the rest of the time series with remarkably similar features and peak values of the recorded forces, as discussed previously. The data however do not provide clear evidence on the ultimate cause of the differences in the separation delay times; whether the divergence originates at a particular angle of attack or after surpassing a certain threshold in the values of the time derivatives of the angle. It is possible that complex boundary layer interactions could explain the responsible underlying mechanism. Further test cases with wider parameter space, field diagnostics such as particle image velocimetry and surface hot-film measurements could give additional insight into the cause.

4.2. Pitch-down motion

At the initial angle of $\alpha = 32°$, a moderately strong suction peak in the first 10% of the airfoil chord indicates a stabilized and attached flow around the leading-edge up to the separation point at approximately $x/c = 0.1$, after which the airfoil exhibits a largely separated flow field (figures 5 and 6e). From this initial condition, the airfoil was pitched down to a final angle of attack of $\alpha = 17°$ utilizing the same three types of motion profiles as in the pitch-up experiments

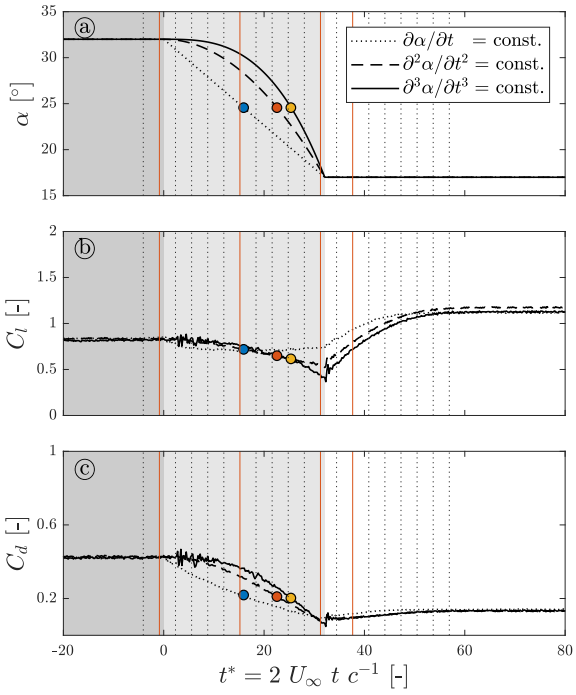

Figure 4. a) The geometric angle of attack α over the non-dimensional time $t^* = 2\ U_\infty\ t\ c^{-1}$ for three different pitch-down motions. Plots b) and c) show the lift and drag coefficients C_l and C_d over time t^*. Colored dots indicate the point in time, when the static stall angle is surpassed. The legend in a) characterizes the motions during the time period highlighted in light gray and applies to all plots. The red vertical lines mark points in time for which the instantaneous pressure distributions are plotted in figure 6e-h.

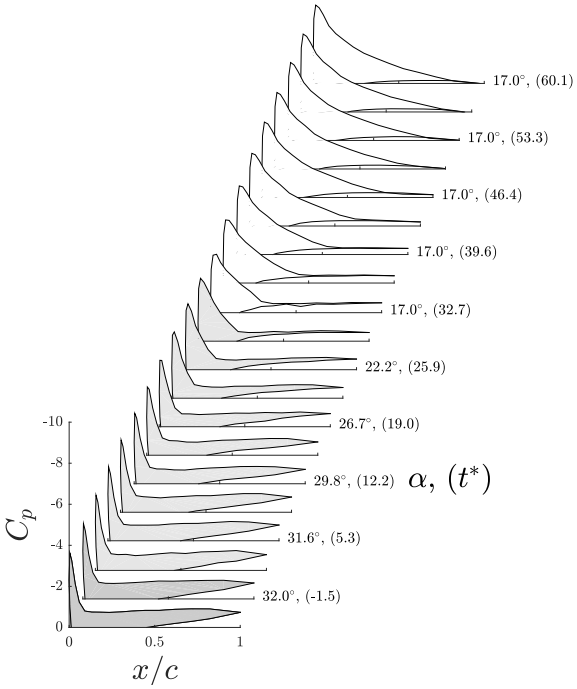

Figure 5. Time series of the suction-side pressure distribution for the pitch-down motion, where the angular acceleration $\partial^2\alpha/\partial t^2 = \text{const.}$ between $0 \leq t^* \leq 31.7$. The color shades correspond to the same time periods highlighted in figure 4. The third axis shows the instantaneous geometric angle of attack α as well as the reduced time t^* in parentheses.

(see figure 4a). During the pitching maneuver the linear case experiences the smallest loss in lift in comparison with the two other cases. The drag values of all three cases are nearly identical at the end of the pitching maneuver; however, the temporal development differs significantly while the airfoil is in motion (figure 4c). After completion of the pitching motion, the recovery to time-independent values is completed within a similar time span for all three cases, despite considerable differences in the lift values at $t^* = 31.7$.

The chronological progression of the boundary layer reattachment process is visualized in plots e-f in figure 6. The lift production with decreasing angle of attack appears to be a result of two counteracting mechanisms, namely the immediate reduction of the suction peak due to lower angles of attack competing against the recovering boundary layer along the chord length of the airfoil. In the linear case, this competition is coincidentally in balance for the particular pitching rate, resulting in a nearly constant lift over time during the pitching maneuver. For the two non-linear cases, with a greater and varying pitching rate $\partial\alpha/\partial t > 0$, the lift production from the suction peak decreases faster than the rising lift production from the recovering boundary

layer, resulting in an overall lift loss. Once the airfoil has reached its final angle of attack of $\alpha = 17°$, the boundary layer fully recovers and with that the lift and drag values converge to steady-state values.

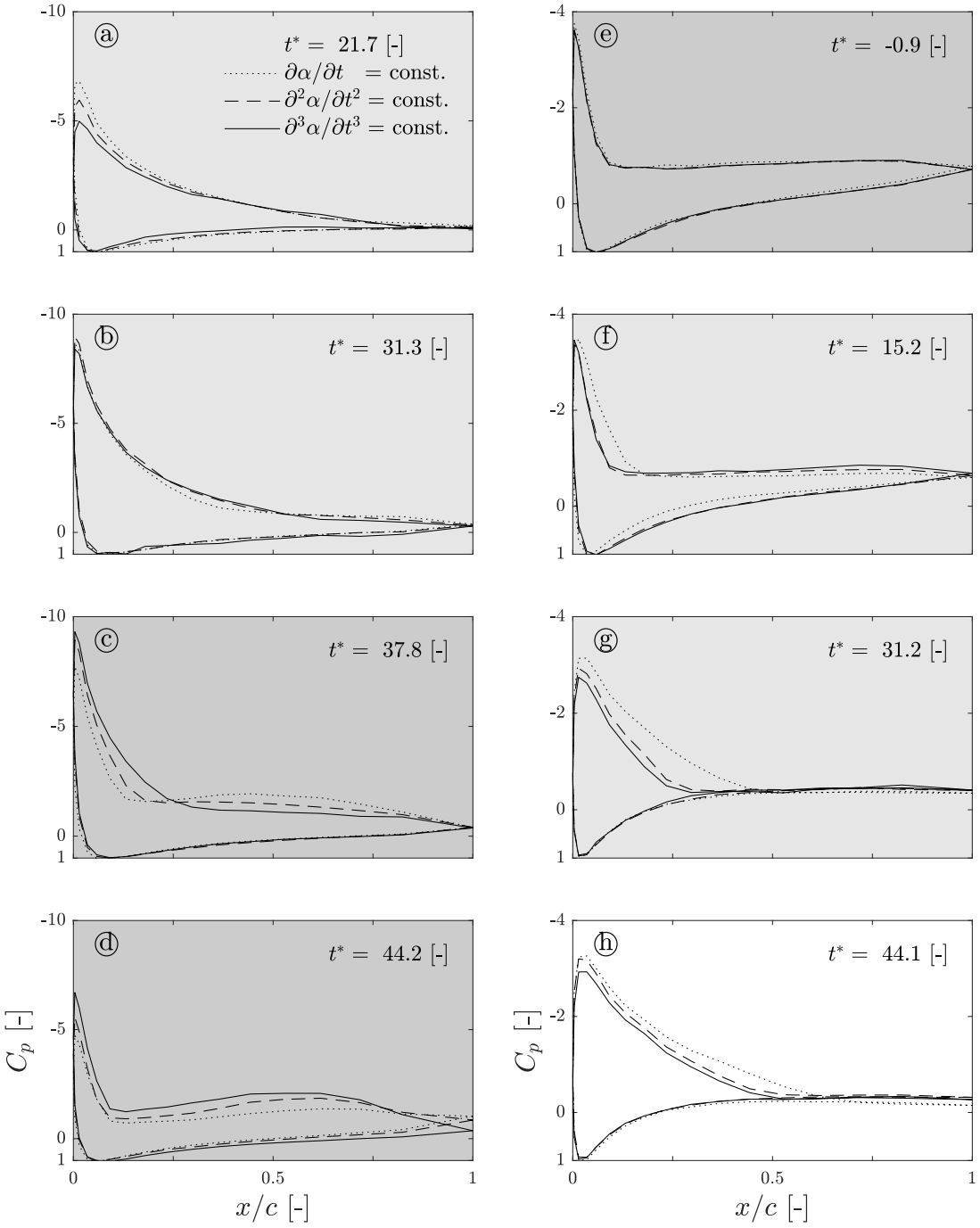

Figure 6. Instantaneous pressure distributions of the pitch-up (a-d) and pitch-down maneuvers (e-h). The specified non-dimensional times correspond to the instants of time highlighted in red in figures 2 and 4. The legend in a) as well as the axes labels apply to all plots and the background colors coincide with highlighted time periods in the previous plots.

5. Conclusions

Phase averaged integrated forces and pressure distributions of a pitching airfoil were experimentally obtained at a chord Reynolds number of three million. The high Reynolds numbers and unsteady conditions were achieved by using a high-pressure wind tunnel which uses compressed air up to 230 bar. High fluid density in combination with low free-stream velocities yield relatively large dimensional time scales yet high Reynolds numbers. The experiments were performed at reduced frequencies within the unsteady range, and unsteady pressure data were acquired using conventional pressure senors.

Two series of ramp tests were conducted for increasing and decreasing angles of attack, each including three test cases of variant types of motion characterized by constant angular velocity, angular acceleration and angular jerk, respectively. The ramp-up experiments revealed a substantial and time-dependent excess of the aerodynamic forces from static values in all three test cases and provided evidence for vortex formation identified in the pressure distributions. Moreover, distinct differences in separation delay times were found in the otherwise similar time series of the forces, when comparing the three test cases. A delayed boundary layer separation process appeared to develop during the ramp-up motion as a consequence of the variant motion types, but no definite explanation for the cause of the varying separation delay could be determined from the data.

Similarly, the ramp-down experiments were largely impacted by the variant types of motion, resulting in distinct differences in the temporal development of the integrated forces. It was found that two counteracting mechanisms were responsible for the deviating force time series, namely the reduction of the suction peak magnitude with decreasing angle of attack competing against a recovering boundary layer on the suction side of the airfoil.

Acknowledgements

The authors would like to thank Dan Hoffman at the Princeton University Gasdynamics lab for his tireless help and great advice in setting up the experiment.

Contributions

J.K. designed the experiment and built the setup. C.E.B. carried out the experiments. J.K. and C.E.B. analyzed the data. J.K. wrote the manuscript. All authors reviewed the paper. M.H. and M.O.L.H. provided scientific advice and contributed to study supervision.

References

[1] van Kuik G A M, Peinke J, Nijssen R, Lekou D, Mann J, Sørensen J N, Ferreira C, van Wingerden J W, Schlipf D, Gebraad P, Polinder H, Abrahamsen A, van Bussel G J W, Sørensen J D, Tavner P, Bottasso C L, Muskulus M, Matha D, Lindeboom H J, Degraer S, Kramer O, Lehnhoff S, Sonnenschein M, Sørensen P E, Künneke R W, Morthorst P E and Skytte K 2016 Long-term research challenges in wind energy – a research agenda by the European Academy of Wind Energy *Wind Energy Science* **1** 1–39 ISSN 2366-7451

[2] Gupta R and Ansell P J 2019 Unsteady flow physics of airfoil dynamic stall *AIAA Journal* **57** 165–175 ISSN 00011452

[3] Rosti M E, Omidyeganeh M and Pinelli A 2016 Direct numerical simulation of the flow around an aerofoil in ramp-up motion *Physics of Fluids* **28** ISSN 10897666

[4] Galbbraith R, Dachun J, Green R, Gracey M and Gilmour R 1992 Collected data for tests on a NACA 0015 aerofoil with chord of length 0.275m Tech. Rep. G.U. Aero Report 9209 University of Glasgow

[5] Leishman J G 2006 *Principles of Helicopter Aerodynamics* 2nd ed (New York City: Cambridge University Press) ISBN 0-521-85860-7

[6] Jiménez J M, Hultmark M and Smits A J 2010 The intermediate wake of a body of revolution at high Reynolds numbers *Journal of Fluid Mechanics* **659** 516–539 ISSN 00221120

[7] Miller M A, Kiefer J, Westergaard C, Hansen M O L and Hultmark M 2019 Horizontal axis wind turbine testing at high Reynolds numbers *Phys. Rev. Fluids*

[8] Miller M A, Duvvuri S, Brownstein I, Lee M, Dabiri J O and Hultmark M 2018 Vertical-axis wind turbine experiments at full dynamic similarity *Journal of Fluid Mechanics* **844** 707–720 ISSN 14697645